Open-Circuit Fault Diagnosis of Rotating Rectifier by Analyzing the Exciter Armature Current

Chenghao Sun, *Student Member, IEEE*, Weiguo Liu, *Senior Member, IEEE*, Zhihuang Wei, *Student Member, IEEE*, Ningfei Jiao, *Member, IEEE*, and Ji Pang, *Student Member, IEEE*

***Abstract*—Based on the differences between waveforms of asynchronous exciter three-phase armature currents with the rotating rectifier under various working conditions (healthy and open-circuit conditions), a fault diagnosis method of rotating rectifier is proposed in this article. To describe these differences, the conceptions of ratio, residual, and sum are defined, and corresponding calculation functions are created. Through the analysis of the asynchronous exciter armature current with the rotating rectifier under five categories of working conditions, three-phase ratios and residuals are calculated by observing which the fault type can be confirmed. Then the faulty diode(s) location is achieved by the sum value. The experimental results show good agreement with theoretical analysis and simulation results, which verifies the feasibility and effectiveness of the proposed method.**

***Index Terms*—Faulty diode location, open-circuit fault diagnosis, rotating rectifier, waveform of current.**

I. Introduction

THE BRUSHLESS wound-rotor synchronous starter/generator (BWSSG) is widely used in many applications, such as aircrafts, submarines, and power plants [1]–[4]. The BWSSG is made up of three parts: an asynchronous exciter (AE), a rotating rectifier, and a main generator (MG), as shown in Fig. 1. Generally, the rotating rectifier mounted on the rotor shaft is a three-phase full-bridge diode rectifier, and fed directly into the filed winding of the MG. Through the rotating rectifier, the AE provides the excitation current for the MG both in the starting and generating modes, which shows that the rectifier plays a significant role in the system [5], [6]. In other words, the diode(s) getting faulty will decrease the output current capability, which may lead to the startup failure and degrade the electricity generation performance.

Manuscript received January 18, 2019; revised June 24, 2019 and September 4, 2019; accepted October 25, 2019. Date of publication November 3, 2019; date of current version February 20, 2020. This work was supported in part by the National Natural Science Foundation of China under Grants 51677152 and 51807165, in part by the Key Research and Development Plan of Shaanxi Province under Grant 2018GY-185, and in part by the Fundamental Research Funds for the Central Universities under Grant 3102019PB004. This paper was presented in part at the IEEE Energy Conversion Congress and Exposition, Portland, OR, USA, September 2018. Recommended for publication by Associate Editor H. Wang. *(Corresponding author: Zhihuang Wei.)*

The authors are with the Shaanxi Key Laboratory of Small and Special Electrical Machine and Drive Technology, School of Automation, Northwestern Polytechnical University, Xi'an 710072, China (e-mail: sunchenghao@mail.nwpu.edu.cn; lwglll@nwpu.edu.cn; wzh_lf@mail.nwpu.edu.cn; jiaoningfei@gmail.com; chickpang@mail.nwpu.edu.cn).

Color versions of one or more of the figures in this article are available online at http://ieeexplore.ieee.org.

Digital Object Identifier 10.1109/TPEL.2019.2951431

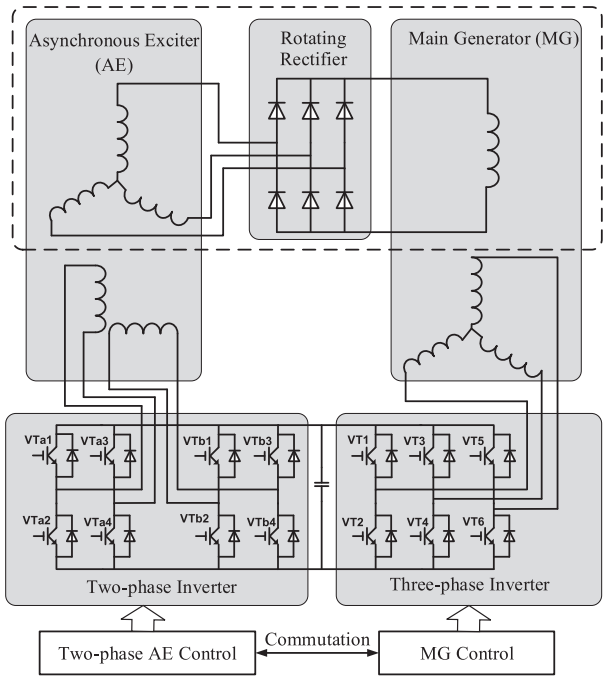

Fig. 1. Structure of the BWSSG.

However, the rotating rectifier is often prone to overvoltage, overcurrent, high temperature, and high-speed-induced centrifugal force [7], [8]. In this case, according to the fault modes, effects, and criticality analysis conducted for the brushless ac generator, the rotating rectifier related faults are one of the highest priority failure modes in BWSSG [9]. The relatively high failure rate has also been witnessed by the research team, that author affiliated with, in practical engineering applications.

Furthermore, the rectifier diodes can fail either in open circuit or short circuit. In practical applications, a short-circuit fault can be converted to an open-circuit fault shortly, which indicates that the open-circuit fault is much more concerned [10], [11]. Consequently, the open-circuit fault diagnosis of the rotating diodes is significant to improve the reliability of the BWSSG.

Although from the aspect of topology, there is no difference between the rotating rectifier and the standard three-phase diodes rectifier (usually in the motionless state), from the aspect of fault diagnosis, difference appears for the signal acquisition. Within the BWSSG, the rotating rectifier is adopted to achieve the brushless structure, which makes the signals on the rotor

side unmeasurable. To be specific, the armature voltages and currents, the output voltage, and the current are unmeasurable. In this case, pressure is imposed on the rotating rectifier fault diagnosis. Majority of the adopted methods for the standard diode rectifier are signal based, namely voltage or current based. For the voltage-based approaches, diode terminal voltage and output voltage are widely used [12]–[16]. Natively, these methods make no sense for the rotating rectifier. By contrast, fewer studies focus on the current-based methods, where the three-phase currents are usually adopted. In [17] and [18], the current Park's vector approach was proposed for the diode rectifier fault diagnosis. However, this method is unable to handle with multiple open-circuit faults and it requires very complex pattern recognition algorithms that are not suitable for the integration into the drive controller and real-time implementation. In [19], on the basis of analyzing the harmonic components of the three-phase currents, Runxia adopted a self-organizing feature map (SOM) network to exact the feature signal in order to achieve fault diagnosis. However, it needs massive calculations, and similar fault types cannot be discriminated for the natural defect of the SOM network.

Beside, at present, the fault diagnosis methods for the rotating rectifier can be divided into the following three categories.

1) Based on the signal processing method: Signal processing can effectively avoid the disadvantages of the modeling and be applied to both nonlinear and linear systems. Among signal processing methods, frequency analysis is widely used. In [20]–[22], by making frequency analysis on the electromotive force of a search coil or a sensor, the working condition of the rotating rectifier can be identified. However, this method may not be useful for the existing BWSSG because it needs to change the structure of BWSSG. Also, by analyzing the harmonic components of the MG stator voltage under different conditions during the generation mode, the side band compared with the fundamental amplitude can be a feature signal for fault diagnosis [11]. Wavelet energy of the MG stator voltage is extracted, and one diode and two diodes open circuit can be detected and classified [23]. This method needs more research when the BWSSG works in the starting mode because the stator windings are powered by the inverter. Fast Fourier transform is performed on the AE field current, the state of rotating rectifier is confirmed [7], but the faulty diode cannot be located. A method is proposed that the third and fundamental components of the estimated armature current could be treated as failure features [5]. Although the location of the faulty diode is not confirmed, this approach is instructive. When the rotating rectifier is under different conditions, the total harmonic distortion of the AE armature current will be different. Combining with the sum of armature current during one cycle, faulty diode can be located [24].
2) Based on the model method [25], [26]: A hybrid modeling approach for brushless generators with nominal and faulty conditions is presented [26]. However, the model for the machine is complex. Besides, topologies between the dc field exciter and the two-phase AE are different.
3) Based on the intelligent algorithm: Some mathematical models of motor are complex and nonlinear. Therefore, building an appropriate model for the machine is challenging. Since the intelligent algorithm can overcome the shortcomings of the model method, an artificial intelligent technology is widely used to conduct the fault diagnosis [27]–[29]. But these methods need many data.

In this article, aiming at uncontrollability of the diode rectifier, the three-phase current characteristics with the rectifier under various faulty conditions are fully studied. On this basis, an open-circuit fault diagnosis method for the rotating rectifier based on the differences between AE armature current waveforms is proposed. The definitions of ratio, residual, and sum are defined and the calculation functions are created to describe the differences. Through the analysis of the AE armature currents with the rectifier under different working conditions, the three-phase ratios and residuals are obtained by which the fault category can be discriminated. Then, the faulty diode(s) location is achieved by the sum value. The experimental results show good agreement with the theoretical analysis and simulation results, which verifies the feasibility and effectiveness of the proposed method.

II. Estimation of AE Armature Current

When the brushless excitation is used, the AE armature current cannot be measured directly, but it can be estimated through the stator flux linkages which are calculated by the AE stator voltages and currents [30].

The exciter is a two-phase AE, in the stator reference frame [31], and the voltage and flux linkage can be expressed as follows:

$$\begin{bmatrix} u_{e\alpha s} \\ u_{e\beta s} \end{bmatrix} = \begin{bmatrix} R_{es} & \\ & R_{es} \end{bmatrix} \begin{bmatrix} i_{e\alpha s} \\ i_{e\beta s} \end{bmatrix} + \mathrm{p} \begin{bmatrix} \lambda_{e\alpha s} \\ \lambda_{e\beta s} \end{bmatrix} \tag{1}$$

and

$$\begin{bmatrix} \lambda_{e\alpha s} \\ \lambda_{e\beta s} \end{bmatrix} = \begin{bmatrix} L_{es} & \\ & L_{es} \end{bmatrix} \begin{bmatrix} i_{e\alpha s} \\ i_{e\beta s} \end{bmatrix} + M_{esr} \times \boldsymbol{\Theta} \begin{bmatrix} -i_{ear} \\ -i_{ebr} \\ -i_{ecr} \end{bmatrix} \tag{2}$$

where

$$\boldsymbol{\Theta} = \begin{bmatrix} \cos\theta_{er} & \cos(\theta_{er} + \frac{2\pi}{3}) & \cos(\theta_{er} - \frac{2\pi}{3}) \\ \sin\theta_{er} & \sin(\theta_{er} + \frac{2\pi}{3}) & \sin(\theta_{er} - \frac{2\pi}{3}) \end{bmatrix}.$$

Considering that the AE rotor windings are "Y" connected, the AE three-phase armature currents have the relation as $i_{ear} + i_{ebr} + i_{ecr} = 0$. Combining (1) and (2), the AE three-phase armature currents can be estimated and expressed as follows:

$$\begin{bmatrix} i_{ear} \\ i_{ebr} \\ i_{ecr} \end{bmatrix} = \frac{1}{3} \begin{bmatrix} -2A_1 & -2A_2 \\ -\sqrt{3}A_2 + A_1 & \sqrt{3}A_1 + A_2 \\ \sqrt{3}A_2 + A_1 & -\sqrt{3}A_1 + A_2 \end{bmatrix} \begin{bmatrix} \cos\theta_{er} \\ \sin\theta_{er} \end{bmatrix} \tag{3}$$

where

$$\begin{bmatrix} A_1 \\ A_2 \end{bmatrix} = \frac{1}{M_{esr}} \begin{bmatrix} \int (u_{e\alpha s} - R_{es} i_{e\alpha s})\, dt - L_{es} i_{e\alpha s} \\ \int (u_{e\beta s} - R_{es} i_{e\beta s})\, dt - L_{es} i_{e\beta s} \end{bmatrix}.$$

In equations above, $u_{e\alpha s}$ and $u_{e\beta s}$ indicate the AE two-phase stator voltages. $i_{e\alpha s}$ and $i_{e\beta s}$ mean the AE stator currents.

i_{ear}, i_{ebr}, and i_{ecr} represent the AE armature currents. R_{es} and L_{es} are the AE stator resistance and inductance, respectively. M_{esr} is the amplitude of the mutual inductance between the stator and armature windings. θ_{er} represents the AE rotor position in the electrical angle. p is a differential operator.

III. Definition of Ratio, Residual, and Sum Functions

The AE armature currents have the same period, no matter which condition the rotating rectifier is under. As mentioned above, the three-phase armature currents can be estimated and the number of current samples in a period is assumed to be L. At the k instant, the sequential data of the three-phase currents collected in discrete time points are shown as follows:

$$I_x(k) = \{i_x(k-L+1), i_x(k-L+2), \ldots, i_x(k)\}$$

where $x = a, b, c$ and i_x indicates the armature current. At every instant, the data are stored and updated as queue. At $k+1$ instant, the sequential data of currents are given as follows:

$$I_x(k+1) = \{i_x(k-L+2), i_x(k-L+3), \ldots, i_x(k+1)\}.$$

Individual current sample $i_x(k)$ can be identified as zero by comparing with the preset threshold K_{th1} which is close to zero, i.e., as follows:

$$N_x(k) = \begin{cases} 1 & |i_x(k)| < K_{\text{th1}} \\ 0 & \text{else.} \end{cases} \tag{4}$$

Then the ratio for one phase that the current is zero during one period is defined as follows:

$$P_x(k) = \frac{1}{L} \sum_{j=k-L+1}^{k} N_x(j). \tag{5}$$

The residual for one phase is defined as follows:

$$R_x(k) = |P_y(k) - P_z(k)| \tag{6}$$

where $x, y, z = a, b, c$ and $x \neq y \neq z$.

Assume that $i_x^{\max}(k)$ indicates the maximum current during one period and $i_x^{\min}(k)$ the minimum. Then, the sum function for one phase is defined as follows:

$$K_x(k) = i_x^{\max}(k) + i_x^{\min}(k). \tag{7}$$

IV. Analysis of Asynchronous Exciter Armature Currents

In practical engineering, usually one diode becomes faulty. Two diodes failing simultaneously is rare, let alone that more than two diodes. Therefore, one diode and two diodes getting open circuit are taken into consideration in this article. To be specific, the working conditions of the rotating rectifier can be grouped into five categories.

1) Heathy condition.
2) One diode is open circuit [such as D1, as shown in Fig. 2(b)].
3) Two diodes located on different legs but the same arm (either upper or lower arm) get open circuit [such as D1 and D3, as shown in Fig. 2(c)].
4) Two diodes located on different legs and arms get open circuit [such as D1 and D6, as shown in Fig. 2(d)].
5) Two diodes located on the same leg get open circuit [such as D1 and D4, as shown in Fig. 2(e)].

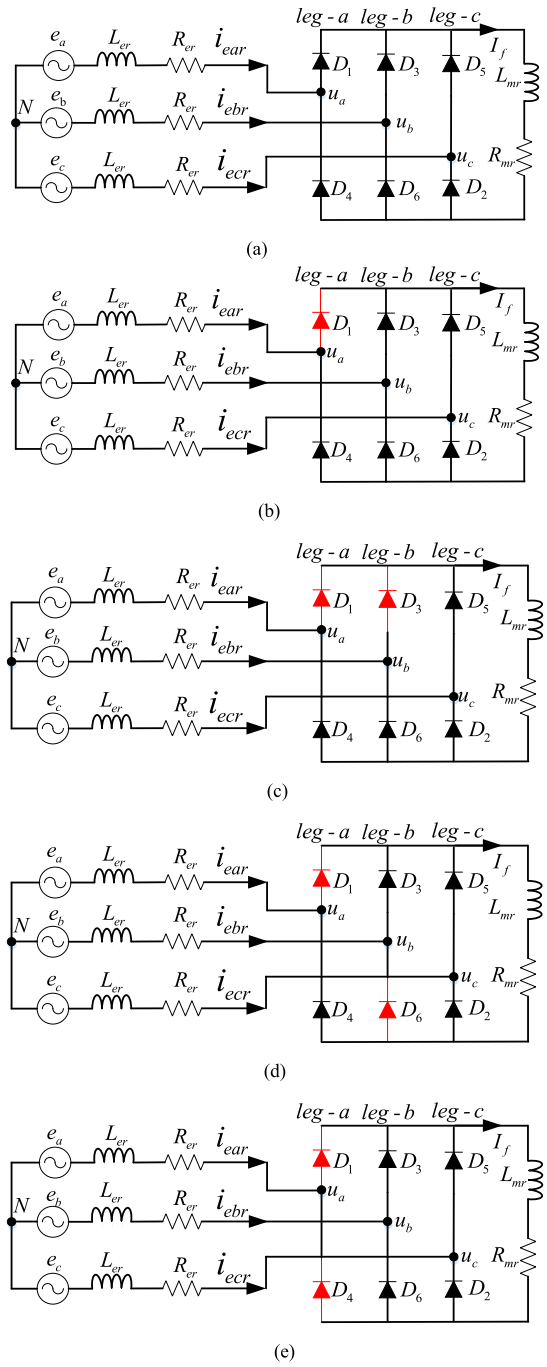

Fig. 2. Equivalent circuits of the BWSSG rotating components with the rectifier under different conditions (open-circuit diode(s) illustrated in red). (a) Healthy condition. (b) Diode D1 fails. (c) Diodes D1 and D3 fail. (d) Diodes D1 and D6 fail. (e) Diodes D1 and D4 fail.

The equivalent circuits of the BWSSG rotating components with the rectifier under different working conditions are shown in Fig. 2.

In practice, the resistance R_{er} of the armature windings has little effect when compared with the reactance $\omega_{er}L_{er}$ [32], where ω_{er} represents the fundamental electrical angular speed

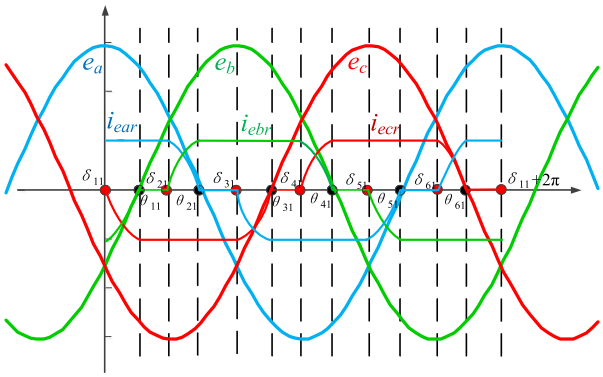

Fig. 3. Diagrams of the AE three-phase armature winding back EMF and current waveforms with the rectifier healthy.

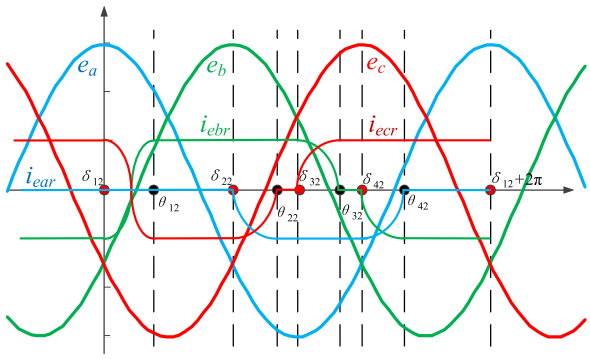

Fig. 4. Diagrams of the AE three-phase armature winding back EMF and current waveforms with D1 open circuit.

of the armature currents. To simplify the analysis, the resistance R_{er} is ignored.

A. Healthy Condition (Denoted as C1)

As shown in Fig. 2(a), when the rotating rectifier is under healthy condition, leg *a*, leg *b*, and leg *c* are healthy. The diagram of the AE three-phase armature current waveforms is shown in Fig. 3, from which the waveforms are found to be symmetric.

Through the analysis, the values for commutation and conduction angles labeled in Fig. 3 are derived as (8). The details of the derivation are shown in the Appendix.

$$\begin{cases} \delta_{21}=\frac{\pi}{3}, \quad \delta_{31}=\frac{2\pi}{3}, \quad \delta_{41}=\pi, \quad \delta_{51}=\frac{4\pi}{3}, \quad \delta_{61}=\frac{5\pi}{3} \\ \theta_{31}=\theta_{11}+\frac{2\pi}{3}, \quad \theta_{41}=\theta_{11}+\pi \\ \theta_{51}=\theta_{11}+\frac{4\pi}{3}, \quad \theta_{61}=\theta_{11}+\frac{5\pi}{3}. \end{cases} \tag{8}$$

Accordingly, the three-phase ratios and residuals during one period are calculated as follows:

$$\begin{cases} P_a=\dfrac{\delta_{31}-\theta_{21}+\delta_{61}-\theta_{51}}{2\pi}=\dfrac{1}{3}-\dfrac{\theta_{11}}{\pi} \\ P_b=\dfrac{\delta_{21}-\theta_{11}+\delta_{51}-\theta_{41}}{2\pi}=\dfrac{1}{3}-\dfrac{\theta_{11}}{\pi} \\ P_c=\dfrac{\delta_{41}-\theta_{31}+\delta_{11}+2\pi-\theta_{61}}{2\pi}=\dfrac{1}{3}-\dfrac{\theta_{11}}{\pi} \end{cases} \tag{9}$$

$$\begin{cases} R_a=|P_b-P_c|=0 \\ R_b=|P_a-P_c|=0 \\ R_c=|P_a-P_b|=0. \end{cases} \tag{10}$$

From (9) and (10), it is demonstrated that the three-phase ratios during one period are the same, and the residuals of ratios are zero, which shows that the three-phase waveforms are symmetric and the rectifier is healthy.

B. Diode D1 Fails (Denoted as C2)

When one diode of the rotating rectifier is open circuit, taking diode D1 as an example shown in Fig. 2(b), leg *a* is faulty, and leg *b* and leg *c* are healthy. The diagrams of the AE armature currents are shown in Fig. 4.

With the same method of analysis, the values for commutation and conduction angles labeled in Fig. 4 are shown as (11). The details of the derivation are shown in the Appendix.

$$\begin{cases} \theta_{32}=\theta_{22}+\frac{\pi}{3}, \quad \theta_{42}=\theta_{22}+\frac{2\pi}{3} \\ \delta_{12}=0, \quad \delta_{22}=\frac{2\pi}{3}, \quad \delta_{32}=\pi, \quad \delta_{42}=\frac{4\pi}{3}. \end{cases} \tag{11}$$

The three-phase ratios together with residuals during one period are expressed as follows:

$$\begin{cases} P_a=\dfrac{\delta_{22}-\delta_{12}+\delta_{12}+2\pi-\theta_{42}}{2\pi}=1-\dfrac{\theta_{22}}{2\pi} \\ P_b=\dfrac{\delta_{42}-\theta_{32}}{2\pi}=\dfrac{1}{2}-\dfrac{\theta_{22}}{2\pi} \\ P_c=\dfrac{\delta_{32}-\theta_{22}}{2\pi}=\dfrac{1}{2}-\frac{\theta_{22}}{2\pi}. \end{cases} \tag{12}$$

and

$$\begin{cases} R_a=|P_b-P_c|=0 \\ R_b=|P_a-P_c|=\frac{1}{2} \\ R_c=|P_a-P_b|=\frac{1}{2}. \end{cases} \tag{13}$$

From (12) and (13), it can be seen that the residual for the only faulty phase *a* is the minimum, while the residuals of healthy phases are the same. Besides, the ratio of the only faulty phase *a* is bigger than that of the healthy phases, which are the same with each other.

C. Diodes D1 and D3 Fail (Denoted as C3)

Under this condition, two diodes from different phases get open circuit and both locate on the upper arm or lower arm. Taking diodes D1 and D3 failing as an example, as shown in Fig. 2(c), leg *c* is healthy, but leg *a* and leg *b* are faulty. The diagrams of the AE three-phase armature winding back electromotive force (EMF) and current waveforms are illustrated in Fig. 5.

The values for commutation and conduction angles labeled in Fig. 5 are shown as (14). Still, the details of the derivation are shown in the Appendix.

$$\begin{cases} \theta_{23}=\theta_{13}+\dfrac{2\pi}{3}, \quad \theta_{33}=\theta_{13}+\dfrac{4\pi}{3} \\ \delta_{13}=0, \ \delta_{23}=\dfrac{2\pi}{3}, \quad \delta_{33}=\dfrac{4\pi}{3}. \end{cases} \tag{14}$$

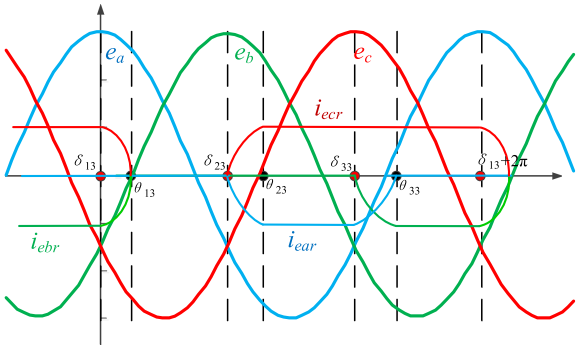

Fig. 5. Diagrams of the AE three-phase armature winding back EMF and current waveforms with D1 and D3 open circuit.

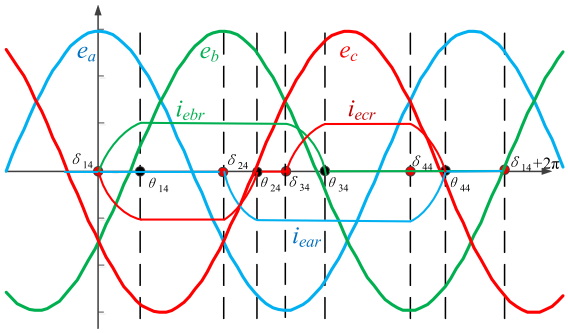

Fig. 6. Diagrams of AE three-phase armature winding back EMF and current waveforms with D1 and D6 open circuit.

The ratios together with the residuals of each phase during the one period are expressed as (15) and (16), respectively.

Equation (16) shows that the residual for the only healthy phase c is the minimum one and that for the faulty phases are bigger but the same with each other. Moreover, the ratio of the only healthy phase c is smaller than that of the faulty phases, which are the same.

$$\begin{cases} P_a = \dfrac{\delta_{23}-\delta_{13}+\delta_{13}+2\pi-\theta_{33}}{2\pi} = \dfrac{2}{3}-\dfrac{\theta_{13}}{2\pi} \\ P_b = \dfrac{\delta_{33}-\theta_{13}}{2\pi} = \dfrac{2}{3}-\dfrac{\theta_{13}}{2\pi} \\ P_c = \dfrac{\delta_{23}-\theta_{13}}{2\pi} = \dfrac{1}{3}-\dfrac{\theta_{13}}{2\pi} \end{cases} \tag{15}$$

$$\begin{cases} R_a = |P_b - P_c| = \dfrac{1}{3} \\ R_b = |P_a - P_c| = \dfrac{1}{3} \\ R_c = |P_a - P_b| = 0. \end{cases} \tag{16}$$

D. Diodes D1 and D6 Fail (Denoted as C4)

As for this condition, two diodes [such as D1 and D6 shown in Fig. 2(d)] from different phases are open circuit, and one diode is on the upper arm, the other is on the lower arm. The diagrams of the AE three-phase armature winding back EMF and current waveforms are shown in Fig. 6. The current of phase a can only be zero or negative, while the current of phase b can only be zero or positive.

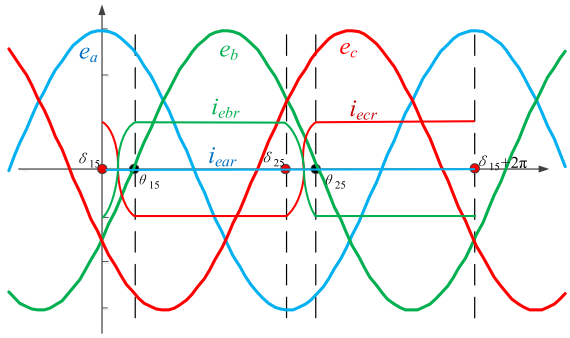

Fig. 7. Diagrams of the AE three-phase armature winding back EMF and current waveforms with D1 and D4 open circuit.

The working states for the rectifier under this condition show great similarity with that under C3 and we get the relations listed as

$$\begin{cases} \theta_{24} = \theta_{14} + \dfrac{2\pi}{3}, \quad \theta_{34} = \theta_{14} + \pi, \quad \theta_{44} = \theta_{14} + \dfrac{5\pi}{3} \\ \delta_{14} = 0, \quad \delta_{24} = \dfrac{2\pi}{3}, \quad \delta_{34} = \pi, \quad \delta_{44} = \dfrac{5\pi}{3}. \end{cases} \tag{17}$$

The three-phase ratios and residuals during one period are expressed as follows:

$$\begin{cases} P_a = \dfrac{\delta_{24}-\delta_{14}+\delta_{14}+2\pi-\theta_{44}}{2\pi} = \dfrac{1}{2}-\dfrac{\theta_{14}}{2\pi} \\ P_b = \dfrac{\delta_{14}+2\pi-\theta_{34}}{2\pi} = \dfrac{1}{2}-\dfrac{\theta_{14}}{2\pi} \\ P_c = \dfrac{\delta_{34}-\theta_{24}+\delta_{14}+2\pi-\theta_{44}}{2\pi} = \dfrac{1}{3}-\dfrac{\theta_{14}}{\pi} \end{cases} \tag{18}$$

$$\begin{cases} R_a = |P_b - P_c| = \frac{1}{6} + \frac{\theta_{14}}{2\pi} \\ R_b = |P_a - P_c| = \frac{1}{6} + \frac{\theta_{14}}{2\pi} \\ R_c = |P_a - P_b| = 0. \end{cases} \tag{19}$$

It can be shown that the residual for the only healthy phase c is the minimum and that for the faulty phases are bigger but the same with each other. Still, the ratio of the only healthy phase c is smaller than that of the faulty phases, which are the same.

E. Diodes D1 and D4 Fail (Denoted as C5)

When two diodes located on the same leg become an open circuit, taking the diodes D1 and D4 for example shown in Fig. 2(e), the diagrams of the AE three-phase armature winding back EMF and current waveforms are shown in Fig. 7.

In this case, the rectifier is equivalent with a single-phase full-bridge rectifier and two commutation points exist during one period. Apparently, the ratios and residuals for three-phases during one period are shown as follows:

$$\begin{cases} P_a = 1 \\ P_b = 0 \\ P_c = 0 \end{cases} \tag{20}$$

$$\begin{cases} R_a = |P_b - P_c| = 0 \\ R_b = |P_a - P_c| = 1 \\ R_c = |P_a - P_b| = 1. \end{cases} \tag{21}$$

TABLE I
FAULT DIAGNOSIS AND FAULTY DIODE(S) LOCATION TABLE ($x, y, z = a, b, c, x \neq y \neq z$)

Condition	Criterion of judgment			Faulty diode(s) location
C1	$R_x(k), R_y(k), R_z(k)<K_{th2}$		×	×
C2	$R_x(k)<K_{th2}$; $R_y(k), R_z(k)>K_{th2}$	$P_x(k)-P_y(k)>0$; $R_{y\ or\ z}(k)<K_{th3}$	$K_x(k)>0$	The lower arm of leg-x
			$K_x(k)<0$	The upper arm of leg-x
C3		$P_x(k)-P_y(k)<0$	$K_y(k), K_z(k)<0$	The upper arm of leg-y and leg-z
			$K_y(k), K_z(k) > 0$	The lower arm of leg-y and leg-z
C4		$P_x(k)-P_y(k)<0$	$K_y(k) <0, K_z(k) >0$	The upper arm of leg-y and lower arm of leg-z
			$K_y(k) >0, K_z(k) < 0$	The lower arm of leg-y and upper arm of leg-z
C5		$P_x(k)-P_y(k)>0$; $R_{y\ or\ z}(k)>K_{th3}$	×	Two diodes of leg-x

From (20) and (21), it can be seen that the residual of ratio for the only faulty phase is the minimum, while the residuals of healthy phases are the same. Meanwhile, the ratio of the only faulty phase is bigger than that of the healthy phases, and the ratios of healthy phases are the same.

It is worth mentioning that, for working conditions C1 and C4, although the armature current analysis is carried out with diode(s) on the upper arm getting open circuit (D1 and D3), it can be easily proved that the analysis with diode(s) on the lower arm getting faulty is equivalent with that on the upper arm which means the same three-phase ratios and residuals.

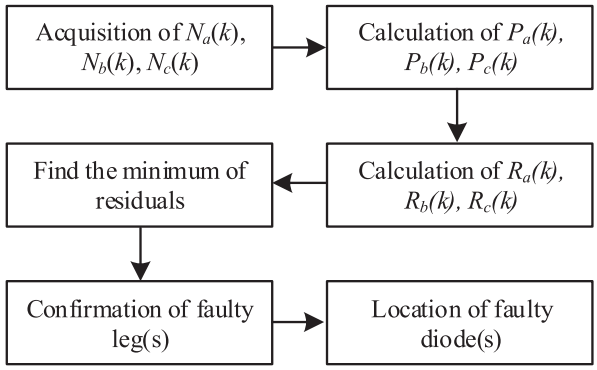

Fig. 8. Flowchart of the open-circuit fault diagnosis method.

V. WORKING CONDITION DISCRIMINATION AND FAULTY DIODE LOCATION

A. Open-Circuit Fault Diagnosis Method

When the rotating rectifier is working under the healthy condition, the waveforms of the AE three-phase armature currents are symmetric. As demonstrated by (9) and (10), the three-phase ratios are same, and the residuals are zero.

However, if the rectifier works in faulty conditions (C2, C3, C4, or C5), from (13), (16), (19), and (21), it can be discovered that there exists the minimum residual among the three-phase residuals. Further, assume the minimum residual as R_x ($x = a, b,$ or c), then leg x is either the only faulty leg (under working conditions C2 or C5) or the only healthy leg (under working conditions C3 or C4).

To further confirm the health condition of leg x (healthy or faulty), it has to resort to the relations between the three-phase ratios. Equations (15) and (18) reveal that if $P_x - P_{y\ \text{or}\ z} < 0$ where $y,\ z = a,\ b,\ c$ and $x \neq y \neq z$, leg x is the only healthy leg, indicating that the rectifier is working under condition C3 or C4.

Otherwise, leg x is the only faulty one, i.e., the rectifier is working under condition C2 or C5. To make further judgement, $R_{y\ \text{or}\ z}$ is used to compare with preset threshold K_{th3} by observing (13) and (21). That is, $R_{y\ \text{or}\ z} < K_{\text{th3}}$ means that the rectifier is working under condition C2 and $R_{y\ \text{or}\ z} > K_{\text{th3}}$ accounts for condition C5.

Moreover, Figs. 4–6 show that the phase current is either zero or negative when the faulty diode locates on the upper arm, and is either zero or positive when the faulty diode locates on the lower arm. Therefore, via the sum value defined as (7), the location of the faulty diode under working conditions C2, C3, and C4 is achieved as follows:

$$\begin{cases} K_{x,y,z}(k) < 0 & \text{faulty diode on the upper arm} \\ K_{x,y,z}(k) > 0 & \text{faulty diode on the lower arm.} \end{cases} \tag{22}$$

It is worth noticing that the discrimination between conditions C3 and C4 is automatically achieved with the location of faulty diode.

Combining with the definitions and calculation of ratios, residuals, and sums in practical application, as stated in Section III, the open-circuit fault diagnosis method is illustrated in Table I and Fig. 8.

B. Decisions of the Threshold

As shown in Fig. 8, the prerequisite for fault diagnosis is the acquisition of $N_x(k)$, defined in (4), where threshold K_{th1} is adopted. The threshold K_{th2} is used to find the minimum among the three-phase residuals and K_{th3} to further discriminate

between conditions C2 and C5, as given in Table I. The decisions of the thresholds are explained as follows.

$K_{\rm th1}$*:* As defined in (4), individual current sample $i_x(k)$ can be identified as zero by comparing with $K_{\rm th1}$ which is zero ideally. However, in practical applications, due to the errors of the measurement and current estimation, $K_{\rm th1}$ is definitely a bit bigger than zero and obviously a experiment-based experienced value. In the experiments of this article, it is found that about 10% of the armature winding current amplitude is a good choice for $K_{\rm th1}$. In this research, $K_{\rm th1}$ is set as 0.5.

$K_{\rm th2}$*:* As for $K_{\rm th2}$, it is used to find the minimum among the three-phase residuals. From (13), (16), (19) and (21), it is found that among the residuals bigger than zero, the minimum residuals are $R_a = R_b = \frac{1}{6} + \frac{\theta_{14}}{2\pi} > \frac{1}{6}$ under working condition C4. So, considering the errors of measurement and current estimation, $K_{\rm th2}$ is set to 0.15 to find the minimum residual. In this case, as given in Table I, $R_x(k),\ R_y(k),\ R_z(k) < K_{\rm th2}$ indicates that the rectifier is healthy, and$R_x(k) < K_{\rm th2}$ together with $R_y(k),\ R_z(k) > K_{\rm th2}$ account for $R_x(k)$ being the minimum.

As given in Table I, $K_{\rm th3}$ is used to discriminate between the working conditions of C2 and C5 by comparing with the residual $R_y(k)$ or $R_z(k)$. Considering the values of R_y or R_z under working conditions C2 and C5 (0.5 and 1, respectively) and the errors of measurement and current estimation, $K_{\rm th3}$ is chosen as 0.75.

VI. Simulation Results

The simulation model of the BWSSG with two-phase AE is built in MATLAB/Simulink. The two-phase AE model is built using the Simscape language based on the voltage and flux linkage equations. As for the rotating rectifier, it is made up of six diodes connected with switches which are from the Simulink library. A resistance in series with an inductance is used to emulate the field winding of the MG. The five working conditions are achieved by the operations of the switches.

The estimated and measured AE armature currents under the healthy and faulty conditions are shown in Figs. 9 and 10. From Figs. 9 and 10, the estimated AE armature currents match well with the measured ones that indicates the effectiveness of the current estimation method.

According to Fig. 8 and Table I, the corresponding postprocessing results of the three-phase ratios, residuals, and sums using the estimated armature currents are shown in Fig. 11.

From Fig. 11(a), under the healthy condition (C1), the three-phase residuals fluctuate around zero and smaller than the threshold $K_{\rm th2}$. However, under faulty conditions, there exists the minimum residual among three-phase residuals. To be specific, R_a being the minimum for $R_a < K_{\rm th2} = 0.15$ occurs when the rectifier works under conditions C2 and C5, and R_c is the minimum for $R_c < K_{\rm th2}$ under conditions C3 and C4.

To further confirm the faulty leg(s), the curve of $P_a - P_c$ is illustrated as Fig. 11(b). It is observed that $P_a - P_c > 0$ happens under conditions C2 and C5, and $P_c - P_a < 0$ exists under conditions C3 and C4.

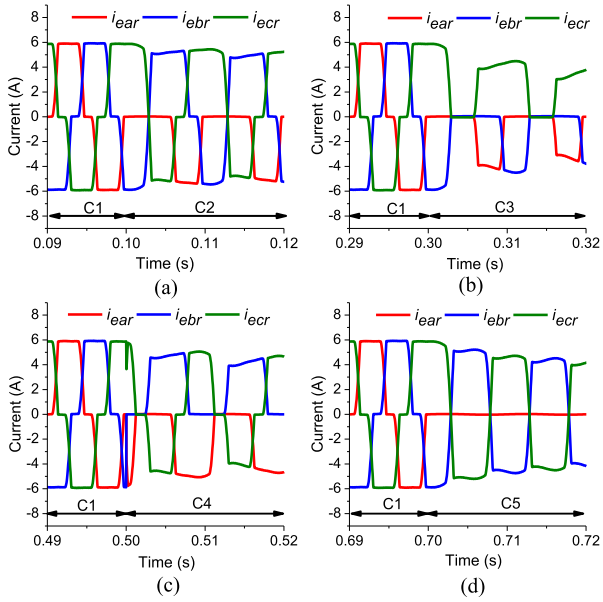

Fig. 9. Estimated AE armature currents with the rotating rectifier under different working conditions.

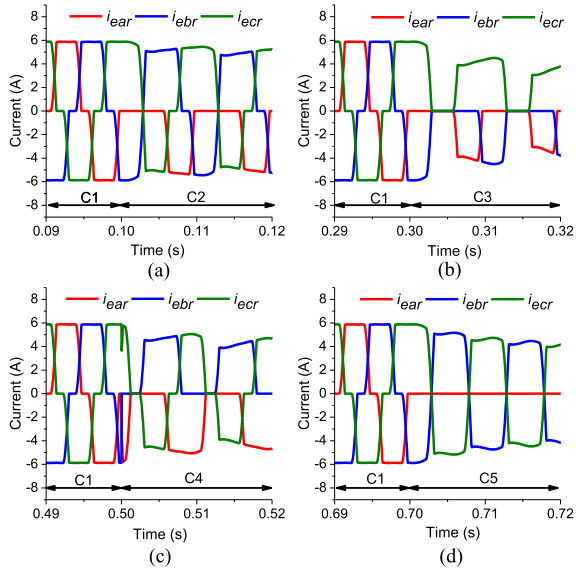

Fig. 10. Measured AE armature currents with the rotating rectifier under different working conditions.

As stated in Section V, the further discrimination between C2 and C5 is a must by comparing $R_{b\text{ or }c}$ and $K_{\rm th3}$. Through Fig. 11(a), it is easily found $R_b < K_{\rm th3} = 0.75$ for condition C2 and $R_b > K_{\rm th3}$ for condition C5.

So far, the confirmation of faulty leg(s) has been done and it is time for faulty diode(s) location. Under condition C2, $K_a < 0$ indicates the faulty diode is on the upper arm, i.e., diode D1 gets open circuit. Similarly, the diodes D1 and D3 get faulty under the condition C3, and the diodes D1 and D6 get faulty under the condition C4.

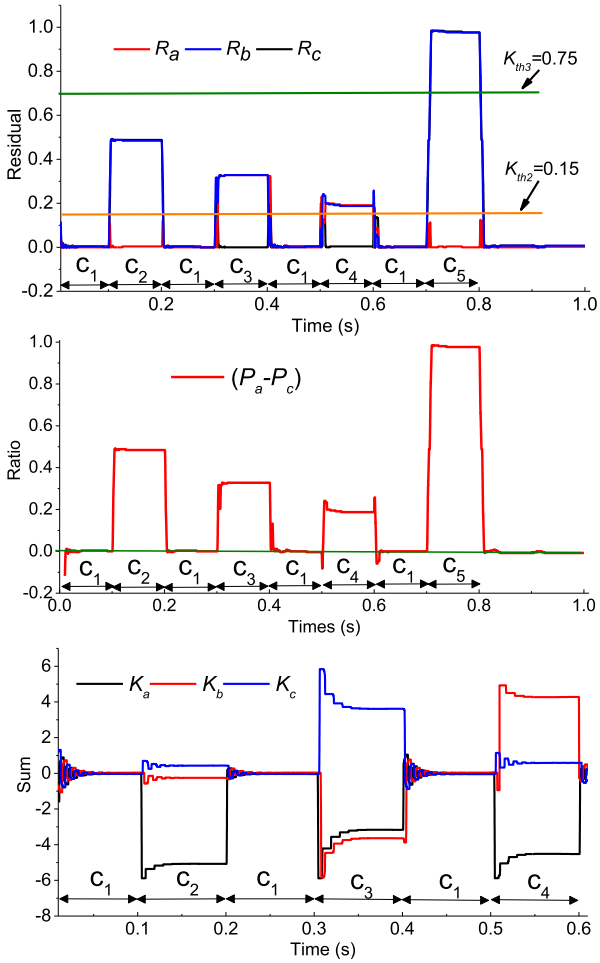

Fig. 11. Curves of postprocessing results of the three-phase ratio, residual, and sum with the rotating rectifier under different working conditions.

Through the discussion above, the simulation results show high agreements with the theoretical analysis and demonstrate the effectiveness of the proposed fault diagnosis method.

VII. Experimental Results

To further verify the effectiveness and feasibility of the proposed method, the experiments are carried out.

A. Experimental Platform

The BWSSG is brushless and the rectifier is mounted on the shaft, which makes the armature currents unmeasurable and the faults of diode(s) cannot be achieved. In this case, a three-phase wound-rotor asynchronous motor with brushes and slip rings is used to emulate the AE in the experiment platform, as shown in Fig. 12. Through the brushes and slip rings, the armature currents can be measured to validate the effectiveness of the current estimation method. Also, a variable frequency modulation asynchronous motor works as the prime motor and a load box emulates the MG field winding. Furthermore, a motionless self-made three-phase rectifier is used to emulate the rotating rectifier to achieve the faulty working conditions. A resistor $R = 7.1\ \Omega$ in series with an inductor $L = 48.08$ mH is adopted to emulate the MG field winding. The fault diagnosis including current estimation is accomplished by the RT-LAB platform, where the model built by MATLAB/Simulink is transformed into real-time codes to be implemented by the real-time simulator. The parameters of the equivalent three-phase AE are listed in Table II.

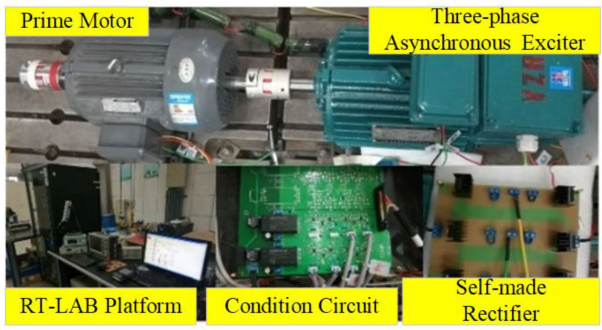

Fig. 12. Experimental platform.

TABLE II
Parameters of Three-Phase AE

Parameters	Values
Stator resistor (R_{es})	4.56 Ω
Rotor resistor (R_{er})	0.45 Ω
Mutual inductance (M_{esr})	52.3 mH
Stator self-inductance (L_{es})	281.3 mH
Rotor self-inductance (L_{er})	23.2 mH
Poles	6

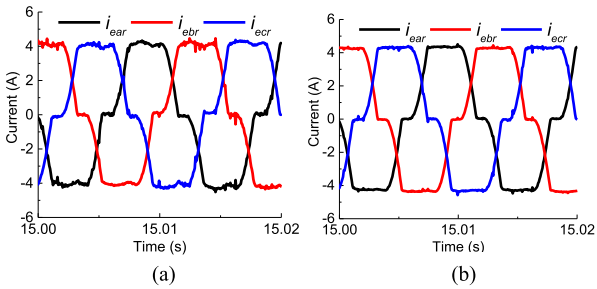

Fig. 13. AE armature currents when the rotating rectifier under the healthy condition (C1). (a) Estimated currents. (b) Measured currents.

B. Experimental Results

Figs. 13–17 illustrate the estimated and measured AE armature currents with the rectifier under different conditions. It is observed that the estimated currents match well with the measured ones which verifies the effectiveness of the current estimation method.

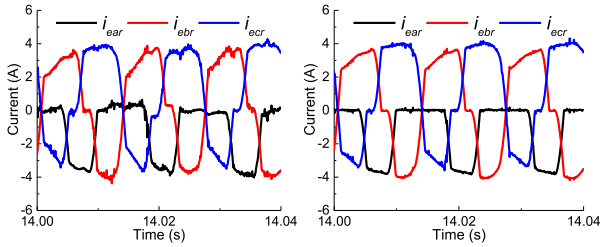

Fig. 14. AE armature currents when diode D1 is open circuit (C2). (a) Estimated currents. (b) Measured currents.

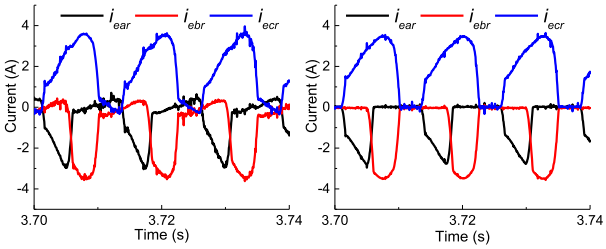

Fig. 15. AE armature currents when diodes D1 and D3 are open circuit (C3). (a) Estimated currents. (b) Measured currents.

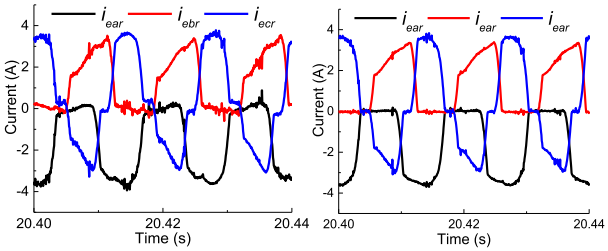

Fig. 16. AE armature currents when diodes D1 and D6 are open circuit (C4). (a) Estimated currents. (b) Measured currents.

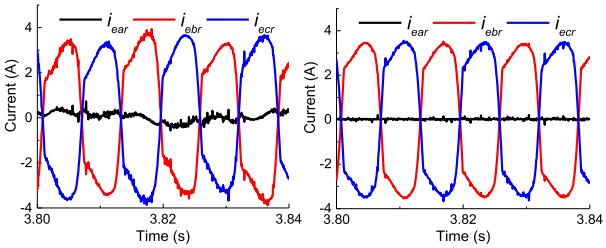

Fig. 17. AE armature currents when diodes D1 and D4 are open circuit (C5). (a) Estimated currents. (b) Measured currents.

Fig. 18 shows that the three-phase ratios are similar and the residuals are smaller than the preset threshold $K_{\rm th2} = 0.15$, indicating the healthy condition.

From Fig. 19(a), R_a is found to be the minimum for being smaller than $K_{\rm th2}$. Then, leg *a* is further confirmed to be the only faulty one by $P_a - P_c > 0$, as shown in Fig. 19(b). Moreover, $R_{b\text{ or }c} < K_{\rm th3} = 0.75$ illustrated in Fig. 19(a) demonstrates that the rectifier is working under the condition C1 but not C5. Finally, $K_a < 0$ shown in Fig. 19(c) indicates that the diode on the upper arm, i.e., D1, gets faulty.

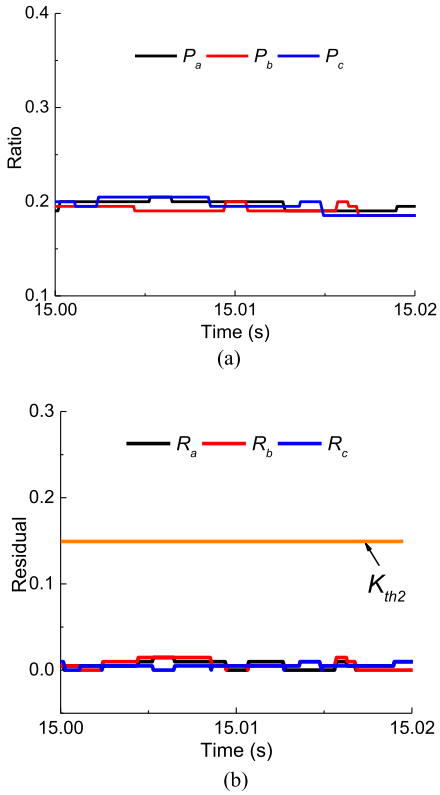

Fig. 18. Three-phase ratios and residuals when the rotating rectifier is under the healthy condition (C1). (a) Ratios. (b) Residuals.

$R_c < K_{\rm th2}$ is found in Fig. 20(a) indicating itself the minimum residual. Then, leg *c* is further confirmed to be the only healthy one by $P_c - P_a < 0$, as shown in Fig. 20(b). Finally, $K_a, K_b < 0$, as shown in Fig. 20(c), indicates that the diodes on the upper arm, i.e., D1 and D3, get faulty.

In Fig. 21(a), $R_c < K_{\rm th2}$ is found indicating itself the minimum residual. Then, leg *c* is further confirmed to be the only healthy one by $P_c - P_a < 0$, as shown in Fig. 21(b). Finally, $K_a < 0$ and $K_b > 0$ as shown in Fig. 21(c) indicates that the diode D1 on the upper arm and D6 on the lower arm fail.

From Fig. 22(a), R_a is found to be the minimum for being smaller than $K_{\rm th2}$. Then, leg *a* is further confirmed to be the only faulty one with $P_a > P_c$, as shown in Fig. 22(b). Moreover, $R_{b\text{ or }c} > K_{\rm th3} = 0.75$ illustrated in Fig. 22(a) demonstrates that the rectifier is working under condition C5 instead of C1, i.e., the diodes D1 and D4 get open circuited.

Through the analysis above, the experimental results show good agreement with the theoretical analysis and simulation results. Therefore, the proposed open-circuit fault diagnosis method is feasible and effective.

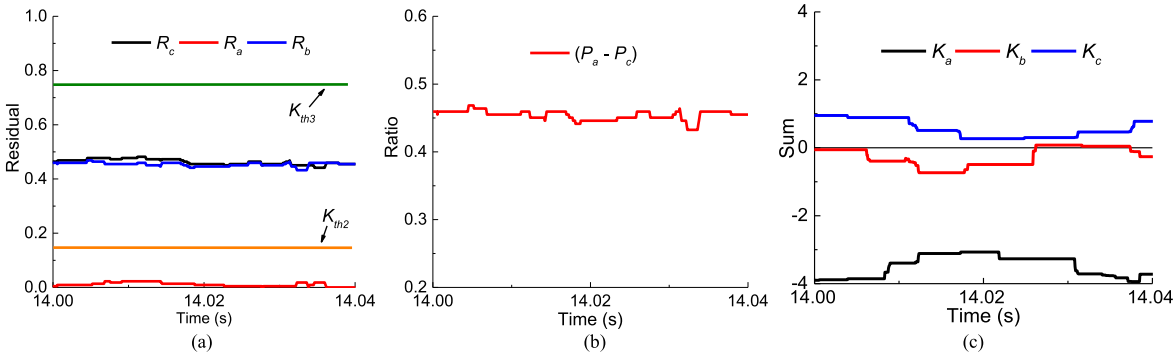

Fig. 19. Three-phase ratios, residuals, and sums when diode D1 is open circuit (C2). (a) Ratios. (b) Residuals. (c) Sums.

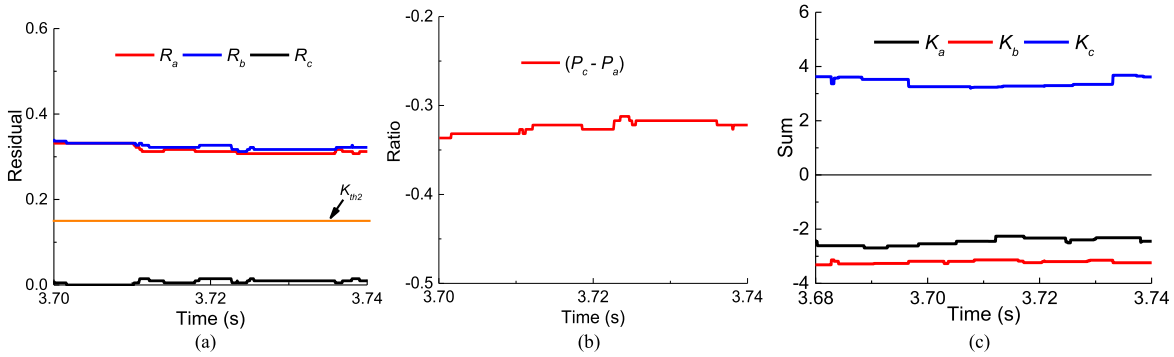

Fig. 20. Three-phase ratios, residuals, and sums when diodes D1 and D3 are open circuit (C3). (a) Ratios. (b) Residuals. (c) Sums.

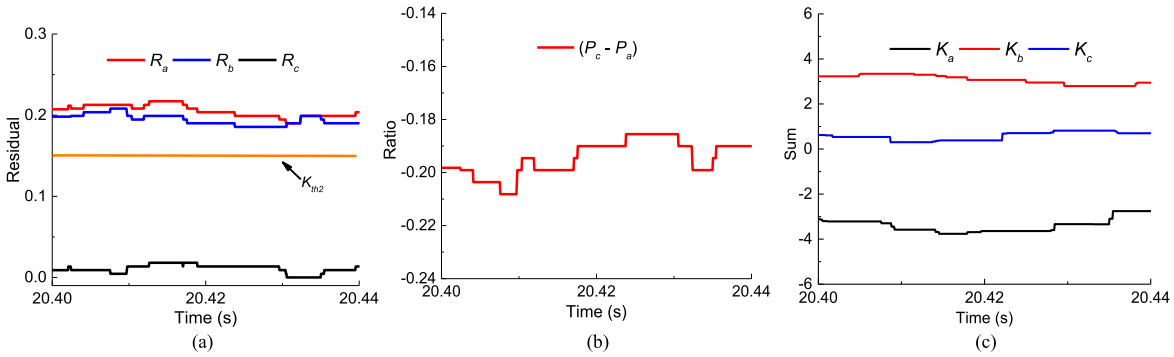

Fig. 21. Three-phase ratios, residuals, and sums when diodes D1 and D6 are open circuit (C4). (a) Ratios. (b) Residuals. (c) Sums.

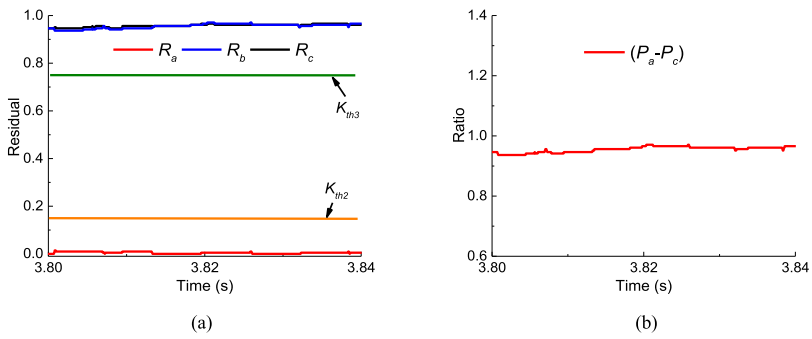

Fig. 22. Three-phase ratios and residuals when diodes D1 and D4 are open circuit (C5). (a) Ratios. (b) Residuals.

VIII. Conclusion

This article presents an open-circuit fault diagnosis method for the rotating rectifier, which is based on the differences between AE armature current waveforms with the rectifier under various working conditions. To describe these fault features, the conceptions of ratio, residual, and sum are proposed, and the corresponding calculation functions are created. Then the analysis of AE armature currents with the rectifier under different working conditions is carried out to obtain the three-phase ratios and residuals, through which the fault category can be confirmed. Then the sum value is used to locate the faulty diode. Finally, the experimental platform is built where experimental results show good agreement with the theoretical analysis and simulation results, verifying the feasibility and effectiveness of the proposed method.

Appendix

Assume the three-phase back EMF is expressed as follows, where E_m represents the amplitude:

$$\begin{cases} e_a = E_m \cos(\omega_{er} t) \\ e_b = E_m \cos\left(\omega_{er} t - \dfrac{2\pi}{3}\right) \\ e_c = E_m \cos\left(\omega_{er} t + \dfrac{2\pi}{3}\right). \end{cases} \tag{23}$$

A. Healthy Condition (Denoted as C1)

It is known that the start of the commutation state is determined by the terminal voltage difference of diodes. Therefore, there are six natural commutation points denoted as $\delta_{11}, \delta_{21}, \delta_{31}, \delta_{41}, \delta_{51}$, and δ_{61}.

As shown in Fig. 3, supposing that the commutation process from phase *b* to phase *c* begins at $\omega_{er} t = \delta_{11}$ and ends at $\omega_{er} t = \theta_{11}$. Obviously, at $\omega_{er} t = \delta_{11}$, neglecting R_{er} we get

$$\begin{cases} u_b = u_c \\ u_b = e_b - \omega_{er} L_{er} \dfrac{di_{ebr}}{d\omega_{er} t} \\ u_c = e_c - \omega_{er} L_{er} \dfrac{di_{ecr}}{d\omega_{er} t}. \end{cases} \tag{24}$$

Combined with $i_{ebr} = -I_f$, $i_{ear} = I_f$, and $i_{ecr} = 0$, $u_b = u_c = e_b = e_c$ is found which indicates $\delta_{11} = 0$. Similarly, we get $\delta_{21} = \frac{\pi}{3}$, $\delta_{31} = \frac{2\pi}{3}$, $\delta_{41} = \pi$, $\delta_{51} = \frac{4\pi}{3}$, $\delta_{61} = \frac{5\pi}{3}$.

In the commutation state, the relations between currents and voltages are shown as follows:

$$\begin{cases} i_{ebr} + i_{ecr} = -I_f, \quad i_{ear} = I_f \\ u_a = e_a, \quad u_b = u_c \\ u_b = e_b - \omega_{er} L_{er} \dfrac{di_{ebr}}{d\omega_{er} t} \\ u_c = e_c - \omega_{er} L_{er} \dfrac{di_{ecr}}{d\omega_{er} t}. \end{cases} \tag{25}$$

By taking $i_{ebr}|_{\omega_{er} t = 0} = -I_f$ into (25), we get

$$i_{ebr} = -I_f + \frac{\sqrt{3} E_m}{\omega_{er} L_{er}} \left[1 - \cos(\omega_{er} t)\right]. \tag{26}$$

At $\omega_{er} t = \theta_{11}$, the commutation state is over. Then by taking $i_{ebr}|_{\omega_{er} t = \theta_{11}} = 0$ into (26), we get

$$\cos(\theta_{11}) = 1 - \frac{2\omega_{er} L_{er} I_f}{\sqrt{3} E_m}. \tag{27}$$

When $\theta_{11} < \omega_{er} t < \delta_{21}$, the rotating rectifier is in the conducting state of phase *a* with phase *c* and the armature currents get the relation as $i_{ear} = I_f$, $i_{ebr} = 0$, and $i_{ecr} = -I_f$.

At $\omega_{er} t = \delta_{21}$, the current commutation process from phase *a* to phase *b* begins and the method of analysis is the same as above. The phase *a* current is expressed as follows:

$$i_{ear} = I_f + \frac{\sqrt{3} E_m}{2\omega_{er} L_{er}} \left[\sin\left(\omega_{er} t + \frac{\pi}{6}\right) - 1\right]. \tag{28}$$

At $\omega_{er} t = \theta_{21}$, the commutation process is over. By taking $i_{ear}|_{\omega_{er} t = \theta_{21}} = 0$ into (28) and combining with (27), we get

$$\begin{cases} \sin\left(\theta_{21} + \dfrac{\pi}{6}\right) = 1 - \dfrac{2\omega_{er} L_{er} I_f}{\sqrt{3} E_m} \\ \theta_{21} = \theta_{11} + \dfrac{\pi}{3}. \end{cases} \tag{29}$$

Similarly, it is found that

$$\begin{aligned} \theta_{31} &= \theta_{11} + \frac{2\pi}{3}, \quad \theta_{41} = \theta_{11} + \pi \\ \theta_{51} &= \theta_{11} + \frac{4\pi}{3}, \quad \theta_{61} = \theta_{11} + \frac{5\pi}{3}. \end{aligned} \tag{30}$$

Finally, we summarize, as in (8).

B. Diode D1 Fails (Denoted as C2)

As mentioned above, the start of the commutation state is determined by the terminal voltage difference of the diodes. However, due to the open circuit of D1, only four commutation points exist during one period. Similarly, neglecting the resistance R_{er}, we get $\delta_{12} = 0$, $\delta_{22} = \frac{2\pi}{3}$, $\delta_{32} = \pi$, $\delta_{42} = \frac{4\pi}{3}$.

When $\delta_{12} = 0 < \omega_{er} t < \theta_{12}$, the rectifier is in the commutation state of phase *b* with phase *c*, and the relations between currents and voltages are expressed as follows:

$$\begin{cases} i_{ebr} + i_{ecr} = 0, \quad i_{ear} = 0 \\ u_a = e_a, \quad u_c = u_b \\ u_b = e_b - \omega_{er} L_{er} \dfrac{di_{ebr}}{d\omega_{er} t} \\ u_c = e_c - \omega_{er} L_{er} \dfrac{di_{ecr}}{d\omega_{er} t}. \end{cases} \tag{31}$$

By taking $i_{ecr}|_{\omega_{er} t = 0} = I_f$ into (31), we get

$$i_{ecr} = I_f + \frac{\sqrt{3} E_m}{2\omega_{er} L_{er}} \left[\cos(\omega_{er} t) - 1\right]. \tag{32}$$

Then take $i_{ecr}|_{\omega_{er} t = \theta_{12}} = -I_f$ into (32), we get

$$\cos(\theta_{12}) = 1 - \frac{4\omega_{er} L_{er}}{\sqrt{3} E_m} I_f. \tag{33}$$

When $\theta_{12} < \omega_{er} t < \delta_{22} = \frac{2\pi}{3}$, the rectifier is in the conduction state of phase *b* and phase *c*. At $\omega_{er} t = \delta_{22} = \frac{2\pi}{3}$, the commutation of phase *a* with phase *c* starts and in the same

way we get

$$i_{ecr} = \frac{\sqrt{3}E_m}{2\omega_{er}L_{er}}\left[1+\cos\left(\omega_{er}t+\frac{\pi}{3}\right)\right] - I_f. \tag{34}$$

Then take $i_{ecr}|_{\omega_{er}t=\theta_{22}} = 0$ into (34), we get

$$\cos\left(\theta_{22}+\frac{\pi}{3}\right) = \frac{2\omega_{er}L_{er}}{\sqrt{3}E_m}I_f - 1. \tag{35}$$

When $\theta_{22} < \omega_{er}t < \delta_{32} = \pi$, the rectifier is in the conduction state with phase *a* and phase *b*. At $\omega_{er}t = \delta_{32} = \pi$, the commutation process from phase *b* to phase *c* begins and similarly we get

$$i_{ebr} = I_f - \frac{\sqrt{3}E_m}{2\omega_{er}L_{er}}\left[1+\cos\left(\omega_{er}t\right)\right]. \tag{36}$$

Then take $i_{ebr}|_{\omega_{er}t=\theta_{32}} = 0$ into (36) and compare with (35), we get

$$\begin{cases} \cos\left(\theta_{32}\right) = \dfrac{2\omega_{er}L_{er}}{\sqrt{3}E_m}I_f - 1 \\ \theta_{32} = \theta_{22} + \dfrac{\pi}{3}. \end{cases} \tag{37}$$

Similarly, we get $\theta_{42} = \theta_{32} + \frac{\pi}{3} = \theta_{22} + \frac{2\pi}{3}$. Finally, we summarize as in (11).

C. Diodes D1 and D3 Fail (Denoted as C3)

In this case, due to the open circuit of D1 and D3, there are only three points during one period where the commutation state starts and with the same analysis method $\delta_{13} = 0,\ \delta_{23} = \frac{2\pi}{3},\ \delta_{33} = \frac{4\pi}{3}$ is obtained.

As illustrated in Fig. 5, the commutation from phase *c* to phase *b* starts at $\omega_{er}t = \delta_{13} = 0$ and stops at $\omega_{er}t = \theta_{13}$ for D1 and D3, failing simultaneously when i_{ebr} approaches 0. The relations between currents and voltages are given as follows:

$$\begin{cases} i_{ebr} + i_{ecr} = 0,\ i_{ear} = 0 \\ u_a = e_a,\ u_c = u_b \\ u_b = e_b - \omega_{er}L_{er}\dfrac{di_{ebr}}{d\omega_{er}t} \\ u_c = e_c - \omega_{er}L_{er}\dfrac{di_{ecr}}{d\omega_{er}t}. \end{cases} \tag{38}$$

Combining (38) with $i_{ecr}|_{\omega_{er}t=\delta_{13}=0} = I_f$, we get

$$i_{ecr} = I_f + \frac{\sqrt{3}E_m}{2\omega_{er}L_{er}}\left[\cos\left(\omega_{er}t\right) - 1\right]. \tag{39}$$

Then take $i_{ecr}|_{\omega_{er}t=\theta_{13}} = 0$ into (39), we get

$$\cos\left(\theta_{13}\right) = 1 - \frac{2\omega_{er}L_{er}}{\sqrt{3}E_m}I_f. \tag{40}$$

When $\delta_{23} < \omega_{er}t < \theta_{23}$, the rectifier is in the commutation state with phase *a* and phase *c* and similarly we get

$$i_{ecr} = \frac{\sqrt{3}E_m}{2\omega_{er}L_{er}}\left[1+\cos\left(\omega_{er}t+\frac{\pi}{3}\right)\right]. \tag{41}$$

Then take $i_{ecr}|_{\omega_{er}t=\theta_{23}} = I_f$ into (41) and compare with (40), we get

$$\begin{cases} \cos\left(\theta_{23}+\dfrac{\pi}{3}\right) = \dfrac{2\omega_{er}L_{er}}{\sqrt{3}E_m}I_f - 1 \\ \theta_{23} = \theta_{13} + \dfrac{2\pi}{3}. \end{cases} \tag{42}$$

Similarly, we get $\theta_{33} = \theta_{13} + \frac{4\pi}{3}$. Finally, it is summarized, as in (14).

REFERENCES

[1] N. Jiao, W. Liu, T. Meng, J. Peng, and S. Mao, "Design and control of a two-phase brushless exciter for aircraft wound-rotor synchronous starter/generator in the starting mode," *IEEE Trans. Power Electron.*, vol. 31, no. 6, pp. 4452–4461, Jun. 2016.

[2] J. Wei, Q. Zheng, and Y. Yang, "Integrated AC and DC excitation method for brushless synchronous machine," in *Proc. IEEE Energy Convers. Congr. Expo.*, Sep. 2012, pp. 2322–2325.

[3] S. Ziaeinejad, Y. Sangsefidi, H. P. Nabi, and A. Shoulaie, "Direct torque control of two-phase induction and synchronous motors," *IEEE Trans. Power Electron.*, vol. 28, no. 8, pp. 4041–4050, Aug. 2013.

[4] N. Jiao, W. Liu, T. Meng, and J. Peng, "Decoupling start control method for aircraft wound-rotor synchronous starter-generator based on main field current estimation," *IET Electr. Power Appl.*, vol. 2018, no. 13, pp. 581–586, Aug. 2018.

[5] Z. Zhang *et al.*, "Identification of TBAES rotating diode failure," *IET Electr. Power Appl.*, vol. 11, pp. 260–271, Feb. 2017.

[6] M. G. McArdle and D. J. Morrow, "Noninvasive detection of brushless exciter rotating diode failure," *IEEE Trans. Energy Convers.*, vol. 19, no. 2, pp. 378–383, Jun. 2004.

[7] J. Y. Liu, K. Gao, and P. F. Liu, "Design and application for fault monitoring circuit of rotating rectifier in aviation brushless AC generator," in *Proc. IEEE Chin. Guid., Navigat. Control Conf.*, Yantai, China, Aug. 8–10, 2014, pp. 1235–1239.

[8] J. Cui, J. Tang, G. Shi, and Z. Zhang, "Generator rotating rectifier fault detection method based on stacked auto-encoder," in *Proc. Workshop Elect. Mach. Des., Control Diagnosis*, 2017, pp. 256–261.

[9] T. D. Batzel and D. C. Swanson, "Prognostic health management of aircraft power generators," *IEEE Trans. Aerosp. Electron. Syst.*, vol. 45, no. 2, pp. 473–482, Apr. 2009.

[10] J. Cui, J. Tang, Z. Zhang, C. Gong, and L. Wang, "Fast fault classification method research of aircraft generator rotating rectifier based on extreme learning machine," *China Elect. Mech. Eng. J.*, vol. 8, pp. 2458–2466, Apr. 2018.

[11] M. Salah, K. Bacha, A. Chaari, and M. E. H. Benbouzid, "Brushless three-phase synchronous generator under rotating diode failure conditions," *IEEE Trans. Energy Convers.*, vol. 29, no. 3, pp. 594–601, Sep. 2014.

[12] M. Rahiminejad, C. Diduch, M. Stevenson, and L. Chang, "Open-circuit fault diagnosis in 3-phase uncontrolled rectifiers," in *Proc. 3rd IEEE Int. Symp. Power Electron. Distrib. Gener. Syst.*, Aalborg, Denmark, 2012, pp. 254–259.

[13] W. Zhu, W. Ma, X. Yang, and H. Xiao, "A fault diagnostic method of 24-Pulse uncontrolled diode rectifier based on the voltage waveform analysis," in *Proc. 2nd Int. Conf. Electron., Netw. Comput. Eng.*, China, 2016, pp. 846–852.

[14] B. Sharan and T. Jain, "Fault diagnosis for open-circuited faults in 3-phase uncontrolled rectifier of wind energy power conversion systems," in *Proc. 15th Int. Conf. Control, Autom. Robot. Vis.*, 2018, pp. 92–97.

[15] J.-U. Lee, S.-W. Baek, K.-Y. Cho, H.-W. Kim, and J.- Choi, "Fault detection of three phase diode rectifier based on harmonic ratio of dc-link voltage ripples," in *Proc. 12th Int. Conf. Power Electron. Drive Syst.*, 2017, pp. 386–391.

[16] M. Iorgulescu, "Study of three-phase bridge rectifier diagnosis based on output voltage and current analysis," in *Proc. 8th Int. Symp. Adv. Topics Elect. Eng.*, 2013, pp. 1–6.

[17] A. J. M. Cardoso and E. S. Saraiva, "On-line condition monitoring of kinetic-electronic systems," in *Proc. Mediterranean Electrotech. Conf.*, 1989, pp. 65–68.

[18] A. J. M. Cardoso and A. M. S. Mendes, "On-line diagnostics of three-phase diode rectifiers, by Park's vector approach," in *Proc. Int. Conf. Elect. Mach.*, 1996, pp. 433–438.

[19] S. Runxia, "Fault diagnosis method of SOM network rectifier circuit with input current harmonics as characteristic," (in Chinese) *Internal Combustion Engine Parts*, vol. 8, pp. 106–110, 2016.
[20] V. Viswanathan, A. K. Gupta, C. J. Gajanayake, and S. Nadarajan, "Rectifier diode fault detection in brushless exciters," Eur. Patent Appl., EP2 908 148, 2015.
[21] X. Y. Li and O. P. Malik, "A microprocessor-based fault monitor for rotating rectifiers of brushless AC exciters using a pattern-recognition approach," *Elect. Mach. Power Syst.*, vol. 24, pp. 189–198, May 1996.
[22] Y. Wu, B. Cai, and Q. Ma, "An online diagnostic method for rotary diode open-circuit faults in brushless exciters," *IEEE Trans. Energy Convers.*, vol. 33, no. 4, pp. 1677–1685, Dec. 2018.
[23] M. Rahnama, A. Vahedi, A. M. Alikhani, and N. Takorabet, "Diode open-circuit fault detection in rectifier bridge of the brushless synchronous generator," in *Proc. Int. Conf. Elect. Mach.*, Oct. 2018, pp. 1821–1826.
[24] Z. Wei, W. Liu, J. Pang, C. Sun, Z. Zhang, and P. Ma, "Fault diagnosis of rotating rectifier based on waveform distortion and polarity of current," in *Proc. IEEE Ind. Appl. Soc. Annu. Meet.*, Sep. 2018, pp. 1–8.
[25] W. Zhang, X. Wu, K. Wei, J. Q. Chen, and N. Lin, "Analysis of bridge-loss fault operation of 12-phase generators with rectifier-load," *Proc. Chin. J. Elect. Eng.*, vol. 36, pp. 1724–1730, Mar. 2016.
[26] R. Isermann, "Model-based fault-detection and diagnosis—Status and applications ☆," *Annu. Rev. Control*, vol. 29, pp. 71–85, 2005.
[27] M. A. Awadallah, "Fuzzy-based on-line detection and prediction of switch faults in the brushless excitation system of synchronous generators," *Electr. Power Compon. Syst.*, vol. 38, pp. 1370–1388, 2010.
[28] D. Gray, Z. Zhang, C. Apostoaia, and C. Xu, "A neural network based approach for the detection of faults in the brushless excitation of a synchronous motor," in *Proc. IEEE Int. Conf. Electro/Inf. Technol.*, Jun. 2009, pp. 423–428.
[29] W. Tao, N. Liu, X. Chi, and K. Sun, "Study of fault diagnosis in brushless machines based on artificial immune algorithm," in *Proc. IEEE Int. Symp. Ind. Electron.*, Jul. 2006, pp. 1779–1782.
[30] P. C. Kjaer, T. Kjellqvist, and C. Delaloye, "Estimation of field current in vector-controlled synchronous machine variable-speed drives employing brushless asynchronous exciters," *IEEE Trans. Ind. Appl.*, vol. 41, no. 3, pp. 834–840, May/Jun. 2005.
[31] N. Jiao, W. Liu, T. Meng, J. Peng, and S. Mao, "Detailed excitation control methods for two-phase brushless exciter of the wound-rotor synchronous starter/generator in the starting mode," *IEEE Trans. Ind. Appl.*, vol. 53, no. 1, pp. 115–123, Jan./Feb. 2017.
[32] D. Liu and J. Fang, "Characteristics of excitation system of rotary rectifier brushless synchronous generator," *Electr. Mach. Control Appl.*, vol. 2, pp. 1–11, Feb. 1979.

Chenghao Sun (S'15) received the B.S. degree from Northwestern Polytechnical University, Xi'an, China, in 2013, where he is currently working toward the Ph.D. degree, all in electrical engineering.

His research interests include design and fault diagnosis of brushless synchronous starter/generator.

Weiguo Liu (SM'07) received the B.S. degree in electrical machines engineering from the Huazhong University of Science and Technology, Wuhan, China, in 1982, the M.S. degree in electrical engineering and the Ph.D. degree in control theory and control engineering from Northwestern Polytechnical University, Xi'an, China, in 1988 and 1999, respectively.

He is currently a Professor with the Department of Electrical Engineering, Northwestern Polytechnical University, and a Guest Professor with the University of Federal Defense, Munich, Germany. He is also the Director of the Institute of Rare Earth Permanent Magnet Electrical Machines and Control Technology, Northwestern Polytechnical University. His research interests include brushless dc machines, PM synchronous machines, dc machines, and induction machines.

Zhihuang Wei (S'17) received the B.S. degree in automation from Xinjiang University, Urumqi, China, in 2016. He is currently working toward the M.S. degree in electrical engineering with Northwestern Polytechnical University, Xi'an, China.

His research interests include fault diagnosis, aircraft starter/generator, and brushless exciters for synchronous machines.

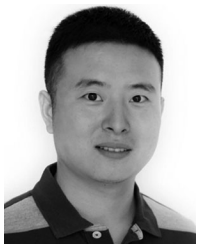

Ningfei Jiao (S'14–M'17) received the B.S. and Ph.D. degrees in electrical engineering from Northwestern Polytechnical University, Xi'an, China, in 2011 and 2017, respectively.

From 2013 to 2014, he was a Visiting Scholar with Michigan Power and Energy Laboratory, University of Michigan, Ann Arbor, MI, USA. He is currently an Associate Researcher with Northwestern Polytechnical University, Xi'an, China. His research interests include aircraft starter/generator and design, analysis, and control of PMSMs.

Ji Pang (S'14) received the B.S. and M.S. degrees from Northwestern Polytechnical University, Xi'an, China, in 2012 and 2015, respectively, where he is currently pursuing the Ph.D. degree, all in electrical engineering.

His research interests include PM machines, aircraft starter/generator, and brushless exciters for synchronous machines.